

Super-Resolution on Rotationally Scanned Photoacoustic Microscopy Images Incorporating Scanning Prior

Kai Pan^{a,1}, Linyang Li^{b,1}, Li Lin^{a,c}, Pujin Cheng^{a,c}, Junyan Lyu^a, Lei Xi^{b,*} and Xiaoyin Tang^{a,c,*}

^athe Department of Electronic and Electrical Engineering, Southern University of Science and Technology, 1088 Xueyuan Avenue, Nanshan District, Shenzhen, 518055, Guangdong, China

^bthe Department of Biomedical Engineering, Southern University of Science and Technology, 1088 Xueyuan Avenue, Nanshan District, Shenzhen, 518055, Guangdong, China

^cJiaying Research Institute, Southern University of Science and Technology, Xiuzhou District, Jiaying, 314000, Zhejiang, China

ARTICLE INFO

Keywords:

Photoacoustic Microscopy
Super-resolution
Rotational Scanning
Odd-and-even Row Registration
Gradient-based Patch Selection

ABSTRACT

Photoacoustic Microscopy (PAM) images integrating the advantages of optical contrast and acoustic resolution have been widely used in brain studies. However, there exists a trade-off between scanning speed and image resolution. Compared with traditional raster scanning, rotational scanning provides good opportunities for fast PAM imaging by optimizing the scanning mechanism. Recently, there is a trend to incorporate deep learning into the scanning process to further increase the scanning speed. Yet, most such attempts are performed for raster scanning while those for rotational scanning are relatively rare. In this study, we propose a novel and well-performing super-resolution framework for rotational scanning-based PAM imaging. To eliminate adjacent rows' displacements due to subject motion or high-frequency scanning distortion, we introduce a registration module across odd and even rows in the preprocessing and incorporate displacement degradation in the training. Besides, gradient-based patch selection is proposed to increase the probability of blood vessel patches being selected for training. A Transformer-based network with a global receptive field is applied for better performance. Experimental results on both synthetic and real datasets demonstrate the effectiveness and generalizability of our proposed framework for rotationally scanned PAM images' super-resolution, both quantitatively and qualitatively. Code is available at <https://github.com/11710615/PAMSR.git>.

1. Introduction

Photoacoustic Microscopy (PAM) imaging provides a novel type of imaging modality that integrates the advantages of both optical contrast and acoustic resolution. This modality has gained increasing recognition in brain studies, particularly in the field of neurovascular and brain metabolism research [41, 16, 29]. As a hybrid imaging technology, PAM detects optical-absorption-induced acoustic signals, enabling direct visualization of the distribution of intrinsic or extrinsic optical absorbers. Compared to other imaging techniques, such as functional magnetic resonance imaging [33, 34] and optical microscopy [31, 52, 14], PAM imaging provides a high resolution, a large field of view (FOV), and a deep penetration depth for real-time imaging of the hemodynamics in intricate brain vascular networks [44, 36, 37]. However, due to the point-scan based imaging mechanism, there is an inevitable trade-off between imaging speed and imaging quality in PAM.

While traditional PAM imaging systems are limited by slow motor scanning [25, 2], recent advances in high-speed PAM imaging have explored faster scanning mechanisms, including galvanometer scanners [42, 17], microelectromechanical systems (MEMS) scanners [4, 12], polygon scanning systems [3, 50], and rotational scanning systems [15, 28, 30]. Among the various techniques available, the rotational scanning system is a noteworthy approach that

seamlessly integrates optical scanning and acoustic detection. This integration facilitates the achievement of coaxial confocal between the laser and ultrasound, resulting in a high signal-to-noise ratio (SNR), large FOV and high-speed imaging without external mechanical scanning, increasing the portability of the system. However, the imaging speed of high-speed PAM systems is often limited by the laser's pulse repetition rate so as to satisfy the optical energy density's safety threshold. And sparse sampling has become a necessary compromise for rotational scanning when there is a need for increasing the imaging speed. Under such a circumstance, applying interpolation algorithms or machine learning methods on sparsely sampled images can further increase the imaging speed.

Image super-resolution (SR) is a process of reconstructing high-resolution (HR) images from low-resolution (LR) inputs. Recently, deep learning (DL) based SR methods have made great strides [39, 43, 19, 18, 21, 47, 8, 27, 48, 7, 26, 6]. Due to the ill-posed attribute of the problem, it is impossible to perfectly recover the original HR image from a given LR image. Based on the different focuses on the quality of the output, SR tasks can be generally classified into PSNR-oriented ones and Perception-oriented ones. PSNR-oriented methods are optimized using pixel-wise losses, resulting in smoother outputs with higher Peak Signal-to-Noise Ratio (PSNR) scores. Perception-oriented methods usually employ GAN losses or other non-reconstruction losses to obtain results that are more visually appealing.

A large number of DL techniques have also been applied in the field of photoacoustic imaging, mainly targeting

*Corresponding authors

✉ xilei@sustech.edu.cn (L. Xi); tangxy@sustech.edu.cn (X. Tang)

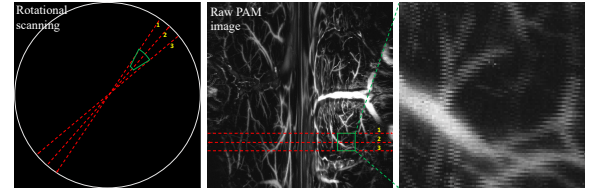
¹Co-first authors: Kai Pan, Linyang Li contributed equally to this work.

imaging acceleration [49, 9, 35], denoising [13], and motion artifact correction [5]. For the imaging acceleration task, the goal is to reconstruct HR images from undersampled ones, with most methods relying on reconstruction-based techniques [9, 35]. Specifically, a binary mask M is used to obtain undersampled PAM images, $I_{lr} = M * I_{hr}$, where $*$ denotes element-wise multiplication and I_{hr} denotes high-resolution images. Although reconstruction-based methods allow arbitrary acceleration scale factors on both image row and image column by designing a specific binary mask M , requiring the input and output of a model of interest to maintain the same shape increases memory cost. Additionally, most methods have been designed to accelerate conventional raster scanning based imaging, with relatively few works considering rotational scanning. In rotational scanning, the scanner moves the transducer along the diameters in the circular scanning area, and all scanning lines are gathered row by row to generate a raw PAM image. Following this, a polar-to-cartesian coordinate transformation is employed to generate the reconstructed image, as illustrated in Fig. 1(a). The number and length of the rows in a raw PAM image respectively represent the number and length of the scanning lines. A position offset may nevertheless exist between the starting point of the current scanning line and the ending point of the last one, leading to displacements across adjacent rows. Furthermore, a reconstructed PAM image may be degraded by a content-independent zero-point mask, as shown in Fig. 1(b). Therefore, it is challenging to directly apply existing DL methods to rotationally scanned undersampled PAM images and there is a strong need for novel and well-performing super-resolution pipelines.

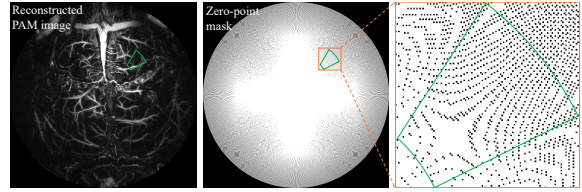
In this study, a novel DL framework is proposed to conduct SR on undersampled raw PAM images obtained through rotational scanning. To address the issue of content-independent zero-point masks and to ensure that our framework aligns with the actual PAM image acquisition process, we apply SR to the raw PAM images but not the reconstructed ones. Additionally, we utilize a Transformer-based architecture for the SR network to endow a larger global receptive field. To reduce displacements across adjacent rows, we implement an even-row-and-odd-row registration module in the preprocessing and incorporate displacement degradation in the training, in which repeated downsampling and upsampling are utilized to simulate displacements for improving blood vessels' continuity in the SR results. We also introduce a constraint on the polar-to-cartesian coordinate transformation by including a consistency loss. Moreover, unlike most natural image SR methods that randomly cut images into patches for training, we use gradient-based patch selection to train on regions with high blood vessel densities.

Our main contributions are summarized as follows:

- We present a novel SR framework based on Vision Transformer for accelerating rotational scanning based PAM imaging.



(a) Raw PAM image with the displacements across adjacent rows



(b) Reconstructed PAM image with zero-point mask

Figure 1: Characteristics of the rotational scanning derived PAM images. As shown in (a), the rotary scanner moves along diameters and gathers scanning lines to form a raw PAM image with obvious displacements across odd-and-even rows. Panel (b) shows the reconstructed result and the content-independent zero-point mask. The rectangle region in the raw PAM image in (a) corresponds to the sector region of the reconstructed result in (b) wherein zero points are likely to appear due to the polar-to-cartesian coordinate transformation.

- In addition to a reconstruction loss, we incorporate a consistency loss to constrain the polar-to-cartesian transformation, resulting in enhanced performance.
- We not only design an even-row-and-odd-row registration module in the preprocessing process but also incorporate displacement degradation in the training process to eliminate displacements and improve blood vessel continuity in the SR results.
- We propose gradient-based patch selection, which forces the network to focus on regions with high densities of blood vessels and accelerates the training convergence.
- We evaluate our method on rotational scanning based PAM images of mouse brains. Results on both synthetic and real undersampled PAM datasets demonstrate the superiority and robustness of our proposed method.

2. Related Work

2.1. Single-image Super-resolution

2.1.1. CNN-based Methods

The single-image SR (SISR) task focuses on recovering HR images from LR counterparts. In recent years, the development of convolutional neural networks (CNNs) has significantly advanced SISR methods. For instance, Ledig *et al.* [18] propose SRResNet, which uses residual blocks to recover fine texture details. Lim *et al.* [21] remove batch normalization layers from residual blocks to prevent

high-frequency components' recovery from being hindered. Zhang *et al.* [48] further design a residual dense block to fully utilize hierarchical features. Zhang *et al.* [47] propose the RCAN model, which combines the channel attention mechanism with residual blocks to adaptively weigh features. Niu *et al.* [27] introduce the holistic attention network, which includes a layer attention module and a channel-spatial attention module to rescale feature weights for informative representations. Dai *et al.* [8] propose a non-locally enhanced residual group to expand the receptive field and emphasize contextual information. Mei *et al.* [26] propose a Pyramid Attention Module that fully utilizes self-similarity across the multi-scale feature and achieves state-of-the-art performance for image restoration tasks.

In addition to the residual and attention module designs, edge information has also been successfully incorporated into SISR methods. For instance, Zhu *et al.* [51] utilize the composition and deformation of existing gradient patterns to estimate HR gradient fields for more reliable SR results. Yang *et al.* [40] propose an edge-based SR approach that embeds prior edge information into the network of interest. Ma *et al.* [24] introduce a gradient reconstruction branch to guide the SR model's training, achieving excellent results in preserving structural similarity. Liang *et al.* [20] propose to employ residual variance to discriminate generated details or artifacts and reduce the weight of artifact regions in the loss, which can be easily incorporated into existing methods and improve performance.

The methods mentioned above have shown impressive results for simple bicubic degradation but have not been widely applied to real-world undersampled situations with complex degradation. As a solution, blind image SR has been developed, wherein the degradation types are unknown. Zhang *et al.* [45] propose a practical degradation model that combines various types of degradation and has achieved remarkable visualization results for real undersampled images. Wang *et al.* [38] introduce a deterministic high-order degradation model to better accommodate real-world situations. Additionally, Luo *et al.* [23] propose a probabilistic degradation model using Generative adversarial networks (GANs) [11] to adaptively learn real degradation distributions.

2.1.2. Transformer-based Methods

The aforementioned CNN methods suffer from limited receptive fields. Recently, Transformer-based frameworks have emerged as state-of-the-art approaches in image reconstruction tasks. Compared with CNNs, Transformers perform better in establishing long-range dependencies and have larger receptive fields. Liang *et al.* [19] apply the Swin-Transformer model [22] to the SR, denoising, JPEG compression, and artifact removing tasks, achieving impressive performance. Wang *et al.* [39] propose a U-shaped Transformer structure with a non-overlapping window-based self-attention mechanism to reduce computation and a multi-scale feature adjustment modulator. Zamir1 *et al.* [43] propose a Restormer model focusing on multi-scale local-global

representation learning, achieving great performance on several image restoration tasks. Chen *et al.* [6] propose a hybrid attention transformer to activate more pixels for image super-resolution. Chen *et al.* [7] apply spatial and channel self-attention in transformer blocks for more powerful feature representation.

In this work, we incorporate gradient-guided prior information into a Transformer-based network to concentrate on edge regions. In contrast to the typical SR approaches which randomly select patches from the input image for model training, our proposed method prioritizes patches with abundant details by increasing their to-be-selected probabilities based on the gradient information. Such a strategy is expected to enhance the overall performance of the model by focusing on image regions that require more attention in the SR process.

2.2. Undersampled PAM Image Reconstruction

PAM image reconstruction plays a crucial role in recovering fully-sampled images from undersampled ones. Traditional interpolation algorithms such as Bicubic and Bilinear interpolation estimate the amplitudes of unsampled points based on their neighbors, which tends to induce distortions. Alternatively, DL-based methods have shown strong representation learning capabilities for undersampled PAM images' reconstruction. For example, a fully dense U-net is applied to reconstruct undersampled PAM images of mouse brains' vasculature at different downsampled rates [9]. Zhou *et al.* [49] use a residual network for optical-resolution PAM (OR-PAM) images' SR. Seong *et al.* [32] for the first time propose a modified SRResNet architecture to reconstruct 3D PAM data. Different from the aforementioned methods that train on paired fully-sampled and synthetic LR images, Vu *et al.* [35] make use of the characteristic that recovery of the noise is slower than that of the content and high-resolution PAM images are obtained by stopping training at a suitable iteration step.

Existing works mentioned above primarily concentrate on reconstructing undersampled PAM images obtained through traditional raster scanning. In contrast, our proposed method is the first to address the super-resolution of high-speed PAM images acquired by rotational scanning. In addition, our approach effectively solves the displacements caused by the rapid scanning process.

3. Methods

The proposed framework is illustrated in Fig. 2. It consists of (1) a data preprocessing module to register adjacent rows' displacements, (2) a patch selection module to select patches with abundant blood vessels to accelerate training, (3) a Transformer-based network to restore high-quality target PAM images, and (4) a consistency loss L_{consis} to ensure structural similarity in the reconstructed PAM images. We below introduce our framework in detail¹.

¹The PAM data collected in our experiments was approved by the ethics committee at the Southern University of Science and Technology: SUSTech-JY202209032.

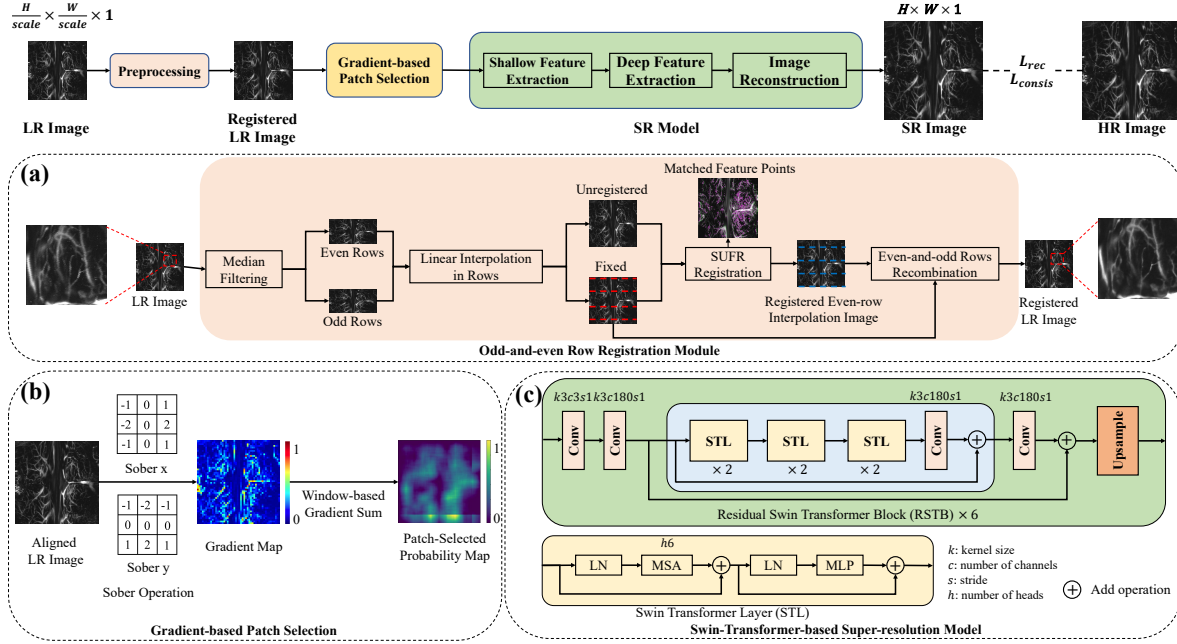


Figure 2: Our proposed framework for PAM image SR. The raw undersampled PAM image is first preprocessed with the median filter and the row registration module to get an aligned LR image, as shown in (a). Then we utilize gradient-based patch selection to select patches with high densities of blood vessels for training, as shown in (b). The SR model consists of shallow feature extraction, deep feature extraction, and image reconstruction steps, as shown in (c). The model is optimized under the combination of a reconstruction loss L_{rec} and a consistency loss $L_{consist}$.

3.1. Odd-and-even Row Registration

In the proposed framework, the odd-and-even row registration module plays a crucial role in eliminating the displacements that occur across adjacent rows in the raw PAM images. To perform the registration, we adopt the Speeded Up Robust Feature (SURF) algorithm. SURF is a feature-based registration method that extracts scale and rotation invariant features using a Hessian-matrix-based blob detector.

The registration process involves several steps, as shown in Fig. 2(a). First, we sample odd rows and even rows from the original image and separately apply linear row interpolation. The odd rows represent the fixed image, while the even rows correspond to the unregistered image. Next, SURF is applied to register the unregistered image to the fixed image, aligning their respective feature points. This registration step ensures that the displacements across adjacent rows are corrected. After the SURF registration, we replace the odd rows in the registered even-row interpolation image with the corresponding odd rows from the fixed image. This step helps to minimize changes or distortions introduced during the registration process. The result is a registered image with minimum displacements and superior alignment across adjacent rows.

When synthesizing the undersampled dataset, after going through registration process to obtain a registered HR image, we directly downsample this registered HR image to generate its paired LR image. For the real undersampled dataset, both the HR image and its corresponding real LR image suffer from displacements across adjacent rows.

Therefore, we apply the SURF registration to both the HR image and the real LR image to obtain a registered HR-LR pair.

3.2. Gradient-based Patch Selection

The patch selection module plays a crucial role in efficiently training the SR network by selecting patches that contain relevant information, such as regions with rich blood vessels. This module helps to speed up the training process and improve the network's ability to learn from informative patches.

To achieve this, the LR image is divided into 64×64 sub-windows and patch selection is performed within each sub-window. The gradient information, which contains high-frequency components that strongly associate with vessel richness, is utilized to assign a score to each sub-window. This score is calculated by applying Sobel operations to each sub-window in both x and y directions. The Sobel operations detect and emphasize edges and gradients in the image. The score for each sub-window is computed as the sum of the gradient scores in both the x and y directions. A higher score indicates a higher likelihood of the sub-window containing blood vessels, which is calculated as below:

$$Score(X_{sub}) = \sum (0.5 * Sober_x(X_{sub}) + 0.5 * Sober_y(X_{sub})), \quad (1)$$

where $Score(X_{sub})$ is the gradient score for sub-window X_{sub} , $Sober_x(\cdot)$ and $Sober_y(\cdot)$ are the Sobel operations applied respectively to x and y directions.

The probability of selecting a sub-window is then determined by normalizing the scores of all sub-windows, formulated as:

$$P(X_{sub}) = \frac{Score(X_{sub})}{\sum_{X_{sub}} Score(X_{sub})}, \quad (2)$$

where $P(X_{sub})$ is the probability for sub-window X_{sub} to be chosen.

Once a sub-window is selected based on its probability, a patch for training is randomly chosen within that window, ensuring that the selected patch contains vessel-rich regions. This process ensures that the network focuses on learning from informative patches.

3.3. Network Architecture

The proposed network architecture is based on a Transformer-based model inspired by SwinIR [19], aiming at capturing both local and global information from PAM images.

The network consists of three main components: shallow feature extraction, deep feature extraction, and image reconstruction, as shown in Fig. 2. Given an input LR image I_{LR} of size $H \times W \times 1$, the shallow feature extraction module is comprised of two convolutional layers. These layers extract local shallow features F_0 of size $H \times W \times C$, where C represents the number of channels.

To capture more global and deeper features, a deep feature extraction module is then applied to the shallow features. This module is composed of a series of Residual Swin Transformer Blocks (RSTBs) and convolutional layers. The RSTBs are designed to capture long-range dependencies and global information by incorporating self-attention mechanisms. The convolutional layers further refine the features and enhance their representation power.

Finally, a reconstruction module is responsible for up-sampling the extracted features and generating the corresponding SR image I_{SR} . Here we employ PixelShuffle to directly upsample images. The whole network is formulated as:

$$F_0 = Conv(I_{LR}), \quad (3)$$

$$F_i = RSTB(F_{i-1}) + F_{i-1}, \quad i = 1, 2, \dots, n, \quad (4)$$

$$F_{deep} = Conv(F_n) + F_0, \quad (5)$$

$$I_{SR} = Rec(F_{deep}), \quad (6)$$

where $Conv(\cdot)$ is a convolutional layer; $F_i (i \geq 1)$ is the i th RSTB module's output while F_0 is the shallow feature; n is the number of RSTB modules; $Rec(\cdot)$ is the reconstruction module.

RSTB contains an even number of cascaded Swin Transformer Layers (STLs), which tails with a convolutional layer in the end. STL calculates multi-head self-attention in a window and employs a shifted window mechanism for window-level feature fusion. In detail, the shallow feature $F_{shallow}$ is split into non-overlapped windows each with a size of $\frac{HW}{hw} \times hw \times C$, where h and w are the window's

height and width. Self-attention (SA) is calculated across pixels within each window as below:

$$Attention(Q, K, V) = softmax(QK^T / \sqrt{d} + B)V, \quad (7)$$

where $Q, K, V \in \mathbb{R}^{n^2 \times d}$ are the *query*, *key*, and *value* matrices projected from the window; B is the learnable position embedding matrix. Window Multi-head Self-attention (WMSA) is performed through parallel attention layers weighed with a parameter matrix. Although WMSA saves lots of computation, there is no connection across windows as attention only represents pixel-wise correlations within the limited-size window. Therefore, Shifted-Window Multi-head Self-attention (SW-MSA) operates window shifting before conducting WMSA. For the aim of strengthening the connection across different windows, WMSA and SWMSA are applied in two continuous STLs, formulated as:

$$X = WMAS(LN(X)) + X, \quad (8)$$

$$X = MLP(LN(X)) + X, \quad (9)$$

$$X = SWMAS(LN(X)) + X, \quad (10)$$

$$X = MLP(LN(X)) + X, \quad (11)$$

where LN represents the layer-norm layer; MLP represents the multi-layer perceptron layer.

3.4. Reconstruction Consistency Loss

A consistency loss L_{consis} is designed to enforce gradient consistency between the reconstructed restored image I_{SR}^{Rec} and the reconstructed fully-sampled ground truth image I_{HR}^{Rec} , particularly in the edge regions. We utilize Sober operators in both x and y directions and calculate the root mean square as the gradient map,

$$GM(I) = \sqrt{(Sober_x(I))^2 + (Sober_y(I))^2}, \quad (12)$$

$$L_{consis} = E\|(GM(I_{SR}^{Rec}) - GM(I_{HR}^{Rec}))\|_1, \quad (13)$$

where $GM(\cdot)$ represents the gradient map.

In addition to the consistency loss L_{consis} for gradient consistency, we utilize a pixel-wise loss L_{rec} which is commonly used in SR tasks,

$$L_{rec} = E\|I_{SR} - I_{HR}\|_1. \quad (14)$$

Therefore, the overall objective function L_{total} is a combination of the pixel-wise loss L_{rec} and the consistency loss L_{consis} , weighed by a trade-off parameter λ as follows:

$$L_{total} = L_{rec} + \lambda L_{consis}. \quad (15)$$

4. Experiments

4.1. Dataset Preparation

We evaluate the performance of our method on two datasets: a synthetic undersampled dataset and a real undersampled dataset. The synthetic undersampled dataset consists of 76 HR images with a resolution of 1000×1000

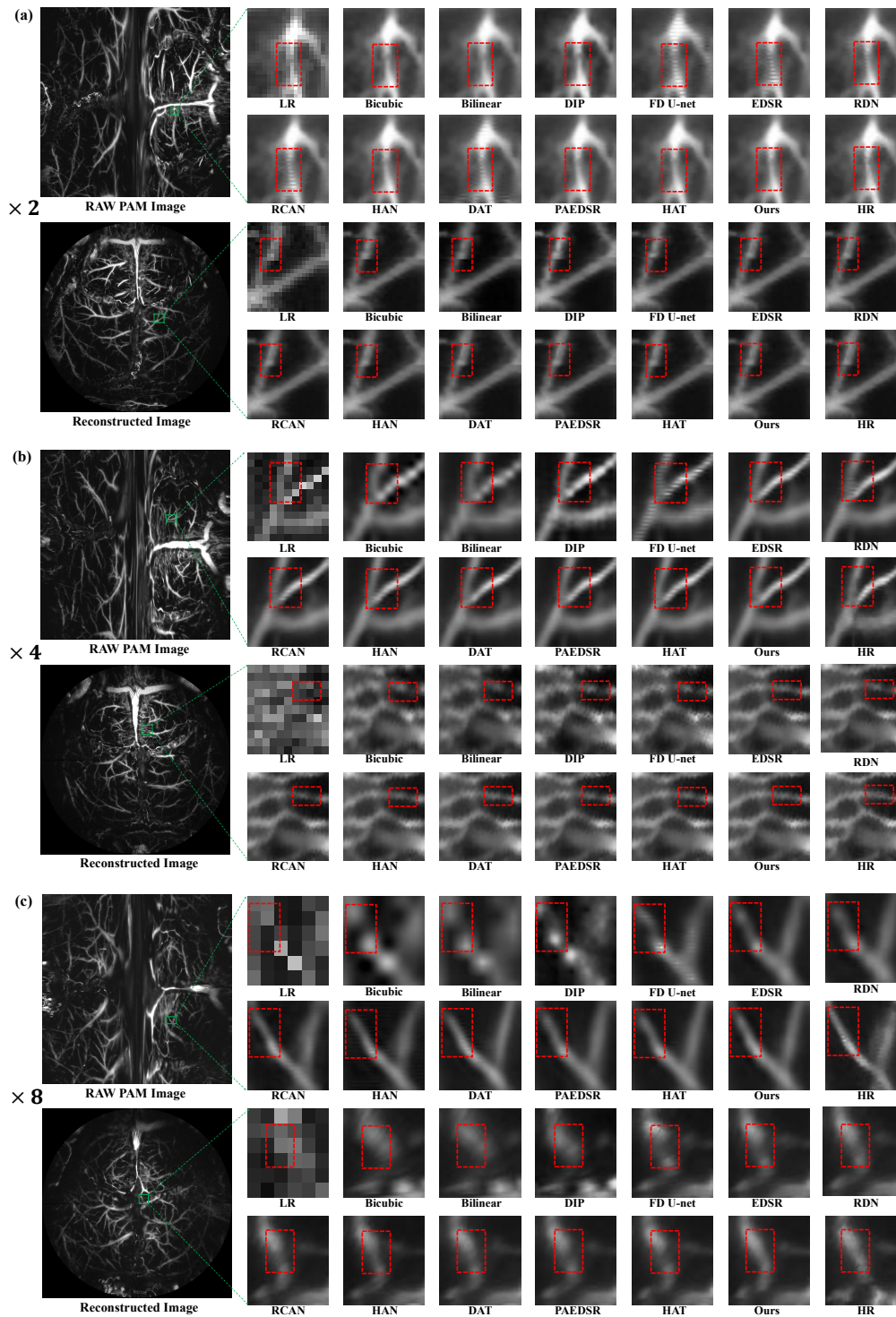


Figure 3: Visual comparisons on synthesized undersampled PAM images with scale factors of 2 in (a), 4 in (b), and 8 in (c). The green rectangle regions are zoomed in and regions with obvious differences are highlighted by red-dotted rectangles.

and the paired LR images are obtained by applying adjacent downsampling to the HR images. The real undersampled dataset consists of 6 paired real LR images with a resolution of 500×500 and the corresponding HR images with a resolution of 1000×1000 ²

²The data is available at this link.

The synthetic undersampled dataset is composed primarily of *in vivo* mouse brain microvasculature data acquired by the Multi-Functional Optical Imaging Lab at Southern University of Science and Technology, using the PAM system previously published in [16]. During each scanning process, we collect 1000 depth-resolved PA signals (A-line) with

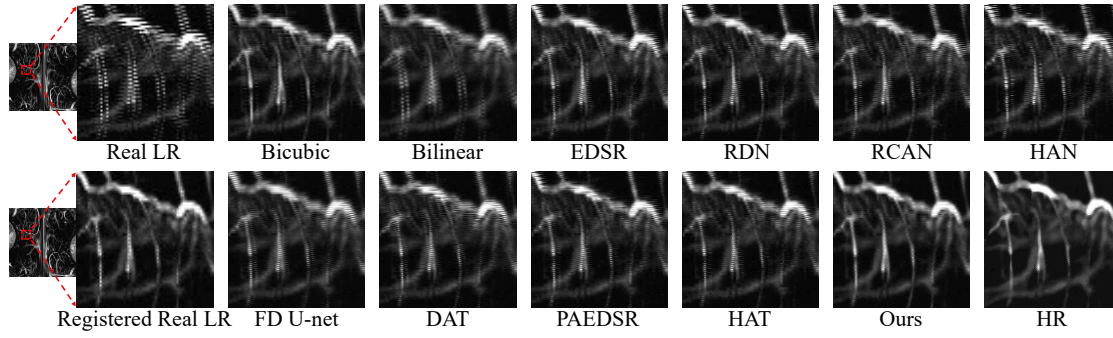


Figure 4: Visual comparisons on real undersampled PAM images at a scale factor of 2. The models pre-trained on the synthetic dataset are directly utilized to test the performance on real undersampled images.

Table 1

Quantitative Evaluations on the synthetic undersampled dataset. The best performance for each metric is highlighted in bold and the second best one is underlined.

Scale	Metrics	Interpolation Methods		Deep Learning Methods								Ours	
		Bicubic	Bilinear	DIP [35] (2021)	FD U-net [9] (2020)	EDSR [21] (2017)	RDN [48] (2018)	RCAN [47] (2018)	HAN [27] (2020)	DAT [7] (2023)	PAEDSR [26] (2023)		HAT [6] (2023)
×2	PSNR ↑	35.121	35.662	30.385	37.202	38.648	39.127	39.261	39.738	<u>40.140</u>	40.104	40.092	41.367
	SSIM ↑	0.959	0.963	0.888	0.971	0.975	0.978	0.980	0.982	<u>0.982</u>	0.982	<u>0.982</u>	0.984
	MSE ↓	22.516	19.905	72.920	14.047	10.369	9.973	9.673	8.180	7.802	7.787	<u>7.732</u>	5.754
	LPIPS ↓	0.0809	0.0792	0.1150	0.0707	0.0430	0.0439	0.0400	0.0379	0.0426	0.0427	0.0405	<u>0.0393</u>
×4	PSNR ↑	28.871	29.181	29.284	30.097	34.152	34.477	33.890	34.176	35.819	35.898	<u>35.958</u>	36.242
	SSIM ↑	0.869	0.876	0.856	0.873	0.942	0.946	0.938	0.945	<u>0.955</u>	<u>0.955</u>	0.956	0.956
	MSE ↓	98.074	88.213	86.007	65.761	29.046	25.214	31.748	29.682	20.117	19.773	<u>19.400</u>	18.113
	LPIPS ↓	0.1329	0.1229	0.1428	0.1282	0.0814	0.0816	0.0805	0.0786	0.0768	0.0826	<u>0.0780</u>	0.0854
×8	PSNR ↑	24.071	24.638	25.052	28.157	28.946	28.921	28.382	28.210	29.192	29.321	<u>29.384</u>	29.519
	SSIM ↑	0.736	0.751	0.728	0.838	0.863	0.858	0.840	0.833	0.866	0.869	0.870	0.873
	MSE ↓	289.885	254.881	216.205	107.896	91.474	92.725	103.856	110.383	87.577	84.969	83.687	81.314
	LPIPS ↓	0.2197	0.2112	0.2430	0.1606	0.1589	0.1607	<u>0.1505</u>	0.1673	0.1472	0.1546	0.1518	0.1527

Table 2

Ablation study on each module on the synthetic undersampled dataset with a scale factor of 2. The best performance for each metric is highlighted in bold and the second best one is underlined.

Rows Reg	Patch Selection	L_{consis}	w.o. Data Aug	PSNR ↑	SSIM ↑	MSE ↓	LPIPS ↓
×	×	×	✓	37.303	0.970	14.970	0.0585
✓	×	×	✓	41.148	<u>0.983</u>	6.001	0.0385
×	✓	✓	✓	37.654	0.971	14.259	0.0583
✓	✓	×	✓	41.292	<u>0.983</u>	5.883	0.0409
✓	×	✓	✓	41.310	<u>0.983</u>	5.801	0.0414
✓	✓	✓	×	37.130	<u>0.969</u>	14.263	0.0707
✓	✓	✓	✓	41.367	0.984	5.754	<u>0.0393</u>

a step interval of $10\mu\text{m}$ in one cross-sectional image (B-scan), and 1000 B-scans with an interval angle of 0.18° to form a volumetric image. Then we carry out maximum amplitude projection to generate a 2D PAM image with a pixel resolution of 1000×1000 . Our dataset contains 76 images of mouse brain vasculature, all acquired at a wavelength of 532nm . We apply a median filter with a kernel size of 3×3 for preprocessing. The data is then randomly divided into approximately 80% (60 images) for training and 20% (16 images) for testing.

Due to subject motion during image acquisition, there are misalignments between the paired LR and HR images in the real undersampled dataset. As a result, it is challenging to directly compare the SR and HR images for this dataset. To address this issue, we leverage the pre-trained model trained

on the synthetic undersampled dataset and apply it to the real LR images. We then evaluate the results qualitatively.

4.2. Implementation Details

The SR model in our framework is based on the architecture of SwinIR [19]. It consists of 6 RSTBs. Within each RSTB, there are 6 STLs, and each STL has 6 attention heads in its MSA. The model utilizes a window size of 8, and self-attention is computed across all pixels within the window. All the convolutional layers' kernel size employed in the model is set as 3. The intermediate feature dimension is set to be 180 for all layers in the model.

During training, the network is optimized using the ADAM optimizer with a learning rate of 10^{-4} , $\beta_1 = 0.9$, $\beta_2 = 0.999$, and $\epsilon = 10^{-8}$ for 200 epochs. The training process utilizes mini-batches of size 8, and each patch is cropped from the training dataset with a size of 64×64 . No data augmentation techniques are applied during training. For scale factors of 4 and 8, the model parameters are initialized with the pre-trained model on the scale factor of 2, except for the upsampling module which is initialized randomly. The weight λ used in the loss function is set to be 0.5 to balance the contributions of the two different components. All models are implemented using the PyTorch framework.

The SURF algorithm used for odd-and-even row registration is implemented using the RegistrationEstimator Toolbox in MATLAB. Its parameters are set as follows: the

number of octaves is set to be 3, and the number of scale levels per octave is set to be 5. We apply nonrigid registration with a smoothing level of 3 and a pyramid level of 1.

To evaluate the effectiveness of our proposed method, we compare it with several baseline algorithms and SISR methods. The baseline algorithms include traditional interpolation methods such as Bicubic and Bilinear interpolations. The SISR methods include EDSR [21], RDN [48], RCAN [47], HAN [27], DAT [7], PAEDSR [26], and HAT [6]. Additionally, we compare our method with two reconstruction-based PAM image acceleration methods, namely FD-Unet [9] and DIP [35]. All compared methods are trained on the unregistered raw PAM images using the hyper-parameters specified in their respective original papers. After obtaining the restored results, we employ the row registration module to align the rows for quantitative and qualitative evaluation. No data augmentation strategies are applied to any of the methods during training.

For quantitative analysis, PSNR, SSIM, MSE, and LPIPS [46] are used to evaluate the performance. PSNR and MSE measure intensity distances between the reconstructed and ground truth images at the pixel level, while SSIM evaluates the structural similarity. LPIPS is used to evaluate perceptual similarity, taking into account human visual perception.

4.3. SR Results on Synthetic Undersampled Data

To evaluate the SR results on the synthetic undersampled dataset, we compute PSNR, SSIM, MSE, and LPIPS between the restored image and the fully sampled ground truth at different scale factors of 2, 4, and 8, as presented in Table. 1. At the scale factor of 2, we find that DIP utilizing image prior to inpaint the undersampled images achieves the worst performance. Although the idea of restoring images without relying on ground truth is promising, displacements across adjacent rows hinder image recovery. In contrast, our proposed method achieves the best performance with PSNR of 41.367 dB, SSIM of 0.984, MSE of 5.754, and LPIPS of 0.0393. As the scale factor increases, all evaluation metrics decline due to the increased difficulty of the task. Nevertheless, our method consistently outperforms all compared methods in terms of all evaluated metrics.

The visual comparisons of the SR results are presented in Fig. 3, wherein results of the scale factors of 2, 4, and 8 are respectively illustrated in sub-figures (a), (b), and (c). In each sub-figure, the first column shows the raw PAM images at the upper half, and the corresponding reconstruction results are displayed at the bottom half. The regions of interest with obvious differences are highlighted using red-dotted rectangles. It is evident that our proposed method achieves superior performance in maintaining vessel continuity and preserving structural details compared to other methods.

4.4. SR Results on Real Undersampled Data

We also evaluate the performance of our method on real undersampled PAM images to assess its generalization capability. Specifically, we utilize the model pre-trained on the synthetic undersampled dataset with a scale factor of

2 to generate SR results. However, it is important to note that both the undersampled and fully-sampled real images suffer from displacements across adjacent rows. We apply the pre-trained $\times 2$ model to the registered real LR images and compare the restored results with the registered HR images. In order to make a fair comparison, the restored results from all other compared methods on unregistered LR images are further registered to align with the HR images. As shown in Fig. 4, post-registration on the restored results cannot effectively eliminate displacements and vessel discontinuity. In contrast, our method, which incorporates pre-registration, exhibits superior performance in terms of vessel continuity without any displacements, and the restored results are visually very close to the HR images. There are no quantitative evaluations provided for the real case due to the poor matching between the real undersampled images and the fully-sampled ones.

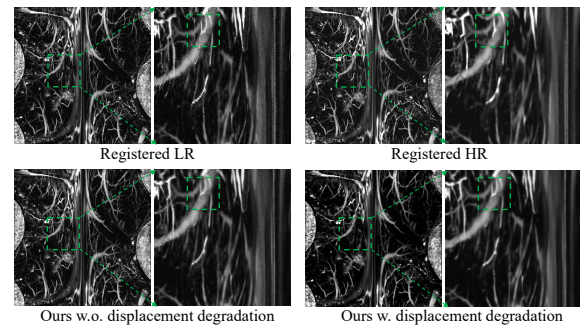


Figure 5: Visual comparisons on real undersampled PAM images between the proposed method trained with and without displacement degradation. The displacements are effectively eliminated when the models are trained using displacement degradation, as indicated by the absence of noticeable differences within the green-dotted rectangles.

4.5. Displacement Degradation based SR Results on Real Undersampled Data

As shown in Fig. 5, we observe that the SR results on real undersampled images still exhibit displacements. This is because the displacements only occur across adjacent rows in real undersampled images, while the synthetic undersampled images with an even downsampling factor do not suffer from this issue. Consequently, when we directly apply the model pre-trained on the synthetic images to the real undersampled images, the displacements persist.

To address this issue, we further perform displacement degradation on the synthetic LR images to force the SR model to eliminate displacements during the restoration process. Specifically, we adopt the approach used in BSRGAN [45] and utilize the same degradation model to synthesize real-world degraded undersampled images. This degradation model consists of a series of degradation steps, including repeated downsampling and upsampling, which can effectively simulate the displacements presented in real undersampled images.

Consequently, we re-train the proposed model on these undersampled images with displacement degradation and evaluate its performance on real undersampled images. As depicted in Fig. 5, when applying the displacement degradation during training, the displacements can be effectively removed from the restored results, and the vessels appear smooth and continuous. This indicates that the model has successfully learned the displacement distribution and effectively eliminated the displacements presented in the real undersampled images.

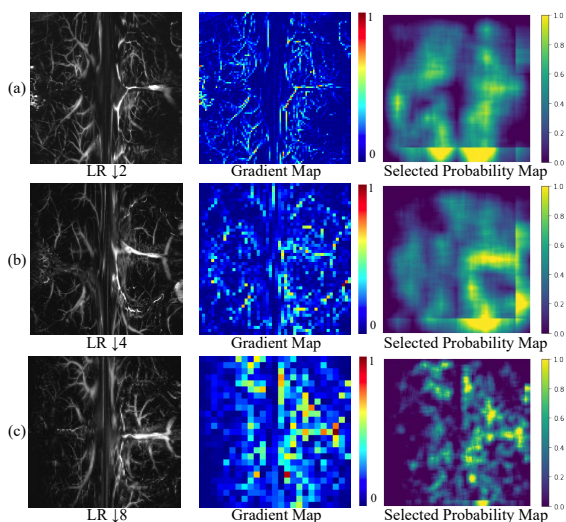


Figure 6: Illustration of the gradient-based patch selection module at the scale factors of 2 in (a), 4 in (b), and 8 in (c). The first column represents the downsampled raw PAM images; the second column represents the normalized Gradient Map calculated from Sober operators; the third column represents the normalized probability of each patch to be selected.

4.6. Ablation Study

4.6.1. Effect of the Odd-and-even Row Registration Module

To assess the importance of the row registration module in our proposed method, we conduct an ablation study by training the method without incorporating the odd-and-even row registration module. Specifically, we synthesize LR-HR pairs by directly downsampling the HR PAM images without performing row registration. In this case, the HR images still contain displacement degradation, while the LR images do not exhibit any displacements.

The quantitative evaluation results, as shown in Table 2, indicate that the proposed method without row registration achieves inferior performance. Specifically, the PSNR reduces by 3.713 dB, the SSIM decreases by 0.013, the MSE increases by 8.505, and the LPIPS rises by 0.019. These results clearly demonstrate that eliminating displacements and ensuring accurate row alignment are crucial preprocessing steps.

4.6.2. Effect of the Patch Selection Module

In Table 2, we also present the ablation analysis results of not employing the patch selection strategy. There is a slight decrease of 0.05 dB in PSNR compared to the proposed pipeline. Compared with the method that only utilizes the row registration module, the incorporation of the patch selection module results in a further improvement of 0.162 dB in PSNR.

The effectiveness of the gradient-based patch selection module is further demonstrated by visualizing the selected probability maps in Fig. 6. The probability map assigns higher probabilities to patches that are more likely to contain relevant information for training, such as regions with abundant vessels in the image of interest. By selectively choosing patches with rich vessel content, the model can learn from more representative and relevant training samples, which leads to enhanced performance in terms of PSNR.

4.6.3. Effect of Data Augmentation

In Table 2, we investigate the influence of rotation augmentation on the performance of our method. Rotation augmentation is a commonly used data augmentation technique in SR tasks to improve models' generalization. However, in our case, we find that rotation augmentation has a negative impact on the performance of our method.

A plausible reason is that the adjacent row registration module in our method aims to eliminate the inherent displacements presented in the ground truth images. However, displacements cannot be completely eliminated, and they still exist to some extent. When applying rotation augmentation, the content-independence regularity of the horizontal displacements is disrupted, leading to weakened performance. Our method without rotation augmentation outperforms the one with rotation augmentation by 4.237 dB in PSNR and 0.015 in SSIM.

5. Conclusion

In this work, we have presented a DL-based framework for the SR of rotationally scanned PAM images. By addressing the issue of adjacent rows' displacements caused by the high-speed rotational scanning, we have introduced an odd-and-even row registration module that can effectively eliminate the displacements in the preprocessing and incorporated displacement degradation in the training, leading to improved vessel continuity in the restored images. Furthermore, we have proposed a gradient-based patch selection module to increase the likelihood of selecting patches with rich vessel information for training, thus improving the overall performance of our SR model. In terms of loss design, we have incorporated a consistency loss L_{consis} , enforcing structural consistency between the reconstructed SR images and the ground truth images. Through extensive experiments on both synthetic and real undersampled datasets at different scale factors, we have demonstrated the effectiveness and robustness of our proposed method.

Our method focuses on the SR of single undersampled PAM image without considering the scenario wherein PAM

images are acquired repeatedly on the same *in-vivo* subject. In future research, we aim to investigate and incorporate such multi-frame approaches, as demonstrated in recent works [1, 10], into our framework to further improve the quality and accuracy of PAM images' SR.

Funding

This study was supported by the National Natural Science Foundation of China (62071210, 62022037, 61775028, 81571722, 61528401); the Shenzhen Basic Research Program (JCYJ20190809120205578); the Shenzhen Science and Technology Program (RCYX20210609103056042, KQTD20190929172743294); the Shenzhen Basic Research Program (JCYJ20200925153847004); the Shenzhen Science and Technology Innovation Committee Program (KCXFZ2020122117340001); the Department of Science and Technology of Guangdong Province (2019ZT08Y191, SZBL2020090501013); the Guangdong Provincial Department of Education (2021ZDZX1064); the Guangdong Provincial Key Laboratory of Advanced Biomaterials (2022B1212010003); the Start-up Grants from Southern University of Science and Technology.

References

- [1] Bhat, G., Danelljan, M., Van Gool, L., Timofte, R., 2021. Deep burst super-resolution, in: Proceedings of the IEEE/CVF Conference on Computer Vision and Pattern Recognition (CVPR), pp. 9209–9218.
- [2] Cao, R., Nelson, S.D., Davis, S., Liang, Y., Luo, Y., Zhang, Y., Crawford, B., Wang, L.V., 2022. Label-free intraoperative histology of bone tissue via deep-learning-assisted ultraviolet photoacoustic microscopy. *Nature Biomedical Engineering*, 1–11.
- [3] Chen, J., Zhang, Y., He, L., Liang, Y., Wang, L., 2020. Wide-field polygon-scanning photoacoustic microscopy of oxygen saturation at 1-mhz a-line rate. *Photoacoustics* 20, 100195.
- [4] Chen, Q., Guo, H., Jin, T., Qi, W., Xie, H., Xi, L., 2018. Ultracompact high-resolution photoacoustic microscopy. *Optics letters* 43, 1615–1618.
- [5] Chen, X., Qi, W., Xi, L., 2019. Deep-learning-based motion-correction algorithm in optical resolution photoacoustic microscopy. *Visual Computing for Industry, Biomedicine, and Art* 2, 1–6.
- [6] Chen, X., Wang, X., Zhou, J., Qiao, Y., Dong, C., 2023a. Activating more pixels in image super-resolution transformer, in: Proceedings of the IEEE/CVF Conference on Computer Vision and Pattern Recognition, pp. 22367–22377.
- [7] Chen, Z., Zhang, Y., Gu, J., Kong, L., Yang, X., Yu, F., 2023b. Dual aggregation transformer for image super-resolution, in: Proceedings of the IEEE/CVF International Conference on Computer Vision, pp. 12312–12321.
- [8] Dai, T., Cai, J., Zhang, Y., Xia, S.T., Zhang, L., 2019. Second-order attention network for single image super-resolution, in: Proceedings of the IEEE/CVF conference on computer vision and pattern recognition, pp. 11065–11074.
- [9] DiSpirito, A., Li, D., Vu, T., Chen, M., Zhang, D., Luo, J., Horstmeyer, R., Yao, J., 2020. Reconstructing undersampled photoacoustic microscopy images using deep learning. *IEEE transactions on medical imaging* 40, 562–570.
- [10] Dudhane, A., Zamir, S.W., Khan, S., Khan, F.S., Yang, M.H., 2022. Burst image restoration and enhancement, in: Proceedings of the IEEE/CVF Conference on Computer Vision and Pattern Recognition (CVPR), pp. 5759–5768.
- [11] Goodfellow, I., Pouget-Abadie, J., Mirza, M., Xu, B., Warde-Farley, D., Ozair, S., Courville, A., Bengio, Y., 2020. Generative adversarial networks. *Communications of the ACM* 63, 139–144.
- [12] Guo, H., Chen, Q., Qin, W., Qi, W., Xi, L., 2021. Detachable head-mounted photoacoustic microscope in freely moving mice. *Optics letters* 46, 6055–6058.
- [13] Haq, I.U., Kawahara, Y., 2020. Convolutional autoencoder-based reconstruction of vascular structures in photoacoustic images, in: *Biomedical Spectroscopy, Microscopy, and Imaging*, SPIE. pp. 193–200.
- [14] Hillman, E.M., Devor, A., Bouchard, M.B., Dunn, A.K., Krauss, G., Skoch, J., Bacskaï, B.J., Dale, A.M., Boas, D.A., 2007. Depth-resolved optical imaging and microscopy of vascular compartment dynamics during somatosensory stimulation. *Neuroimage* 35, 89–104.
- [15] Jin, T., Guo, H., Jiang, H., Ke, B., Xi, L., 2017. Portable optical resolution photoacoustic microscopy (porpam) for human oral imaging. *Optics letters* 42, 4434–4437.
- [16] Jin, T., Qi, W., Liang, X., Guo, H., Liu, Q., Xi, L., 2022. Photoacoustic imaging of brain functions: Wide filed-of-view functional imaging with high spatiotemporal resolution. *Laser & Photonics Reviews* 16, 2100304.
- [17] Kim, J., Kim, J.Y., Jeon, S., Baik, J.W., Cho, S.H., Kim, C., 2019. Super-resolution localization photoacoustic microscopy using intrinsic red blood cells as contrast absorbers. *Light: Science & Applications* 8, 103.
- [18] Ledig, C., Theis, L., Huszár, F., Caballero, J., Cunningham, A., Acosta, A., Aitken, A., Tejani, A., Totz, J., Wang, Z., et al., 2017. Photo-realistic single image super-resolution using a generative adversarial network, in: Proceedings of the IEEE conference on computer vision and pattern recognition, pp. 4681–4690.
- [19] Liang, J., Cao, J., Sun, G., Zhang, K., Van Gool, L., Timofte, R., 2021. Swinir: Image restoration using swin transformer, in: Proceedings of the IEEE/CVF International Conference on Computer Vision, pp. 1833–1844.
- [20] Liang, J., Zeng, H., Zhang, L., 2022. Details or artifacts: A locally discriminative learning approach to realistic image super-resolution, in: Proceedings of the IEEE/CVF Conference on Computer Vision and Pattern Recognition, pp. 5657–5666.
- [21] Lim, B., Son, S., Kim, H., Nah, S., Mu Lee, K., 2017. Enhanced deep residual networks for single image super-resolution, in: Proceedings of the IEEE conference on computer vision and pattern recognition workshops, pp. 136–144.
- [22] Liu, Z., Lin, Y., Cao, Y., Hu, H., Wei, Y., Zhang, Z., Lin, S., Guo, B., 2021. Swin transformer: Hierarchical vision transformer using shifted windows, in: Proceedings of the IEEE/CVF International Conference on Computer Vision, pp. 10012–10022.
- [23] Luo, Z., Huang, Y., Li, S., Wang, L., Tan, T., 2022. Learning the degradation distribution for blind image super-resolution, in: Proceedings of the IEEE/CVF Conference on Computer Vision and Pattern Recognition, pp. 6063–6072.
- [24] Ma, C., Rao, Y., Cheng, Y., Chen, C., Lu, J., Zhou, J., 2020. Structure-preserving super resolution with gradient guidance, in: Proceedings of the IEEE/CVF conference on computer vision and pattern recognition, pp. 7769–7778.
- [25] Maslov, K., Zhang, H.F., Hu, S., Wang, L.V., 2008. Optical-resolution photoacoustic microscopy for in vivo imaging of single capillaries. *Optics letters* 33, 929–931.
- [26] Mei, Y., Fan, Y., Zhang, Y., Yu, J., Zhou, Y., Liu, D., Fu, Y., Huang, T.S., Shi, H., 2023. Pyramid attention network for image restoration. *International Journal of Computer Vision*, 1–19.
- [27] Niu, B., Wen, W., Ren, W., Zhang, X., Yang, L., Wang, S., Zhang, K., Cao, X., Shen, H., 2020. Single image super-resolution via a holistic attention network, in: European conference on computer vision, Springer. pp. 191–207.
- [28] Qi, W., Jin, T., Rong, J., Jiang, H., Xi, L., 2017. Inverted multiscale optical resolution photoacoustic microscopy. *Journal of biophotonics* 10, 1580–1585.

- [29] Qin, W., Gan, Q., Yang, L., Wang, Y., Qi, W., Ke, B., Xi, L., 2021. High-resolution in vivo imaging of rhesus cerebral cortex with ultrafast portable photoacoustic microscopy. *NeuroImage* 238, 118260.
- [30] Qin, W., Qi, W., Xi, L., 2019. Quantitative investigation of vascular response to mesenteric venous thrombosis using large-field-of-view photoacoustic microscopy. *Journal of Biophotonics* 12, e201900198.
- [31] Sakadžić, S., Roussakis, E., Yaseen, M.A., Mandeville, E.T., Srinivasan, V.J., Arai, K., Ruvinskaya, S., Devor, A., Lo, E.H., Vinogradov, S.A., et al., 2010. Two-photon high-resolution measurement of partial pressure of oxygen in cerebral vasculature and tissue. *Nature methods* 7, 755–759.
- [32] Seong, D., Lee, E., Kim, Y., Han, S., Lee, J., Jeon, M., Kim, J., 2023. Three-dimensional reconstructing undersampled photoacoustic microscopy images using deep learning. *Photoacoustics* 29, 100429.
- [33] Toga, A.W., Thompson, P.M., Mori, S., Amunts, K., Zilles, K., 2006. Towards multimodal atlases of the human brain. *Nature Reviews Neuroscience* 7, 952–966.
- [34] Uludağ, K., Blinder, P., 2018. Linking brain vascular physiology to hemodynamic response in ultra-high field mri. *Neuroimage* 168, 279–295.
- [35] Vu, T., DiSpirito III, A., Li, D., Wang, Z., Zhu, X., Chen, M., Jiang, L., Zhang, D., Luo, J., Zhang, Y.S., et al., 2021. Deep image prior for undersampling high-speed photoacoustic microscopy. *Photoacoustics* 22, 100266.
- [36] Wang, L.V., Hu, S., 2012. Photoacoustic tomography: in vivo imaging from organelles to organs. *science* 335, 1458–1462.
- [37] Wang, L.V., Yao, J., 2016. A practical guide to photoacoustic tomography in the life sciences. *Nature methods* 13, 627–638.
- [38] Wang, X., Xie, L., Dong, C., Shan, Y., 2021. Real-esrgan: Training real-world blind super-resolution with pure synthetic data, in: *Proceedings of the IEEE/CVF International Conference on Computer Vision*, pp. 1905–1914.
- [39] Wang, Z., Cun, X., Bao, J., Zhou, W., Liu, J., Li, H., 2022. Uformer: A general u-shaped transformer for image restoration, in: *Proceedings of the IEEE/CVF Conference on Computer Vision and Pattern Recognition*, pp. 17683–17693.
- [40] Yang, W., Feng, J., Yang, J., Zhao, F., Liu, J., Guo, Z., Yan, S., 2017. Deep edge guided recurrent residual learning for image super-resolution. *IEEE Transactions on Image Processing* 26, 5895–5907.
- [41] Yao, J., Wang, L., Yang, J.M., Maslov, K.I., Wong, T.T., Li, L., Huang, C.H., Zou, J., Wang, L.V., 2015. High-speed label-free functional photoacoustic microscopy of mouse brain in action. *Nature methods* 12, 407–410.
- [42] Yuan, Y., Yang, S., Xing, D., 2012. Optical-resolution photoacoustic microscopy based on two-dimensional scanning galvanometer. *Applied Physics Letters* 100, 023702.
- [43] Zamir, S.W., Arora, A., Khan, S., Hayat, M., Khan, F.S., Yang, M.H., 2022. Restormer: Efficient transformer for high-resolution image restoration, in: *Proceedings of the IEEE/CVF Conference on Computer Vision and Pattern Recognition*, pp. 5728–5739.
- [44] Zhang, H.F., Maslov, K., Stoica, G., Wang, L.V., 2006. Functional photoacoustic microscopy for high-resolution and noninvasive in vivo imaging. *Nature biotechnology* 24, 848–851.
- [45] Zhang, K., Liang, J., Van Gool, L., Timofte, R., 2021. Designing a practical degradation model for deep blind image super-resolution, in: *Proceedings of the IEEE/CVF International Conference on Computer Vision*, pp. 4791–4800.
- [46] Zhang, R., Isola, P., Efros, A.A., Shechtman, E., Wang, O., 2018a. The unreasonable effectiveness of deep features as a perceptual metric, in: *Proceedings of the IEEE conference on computer vision and pattern recognition*, pp. 586–595.
- [47] Zhang, Y., Li, K., Li, K., Wang, L., Zhong, B., Fu, Y., 2018b. Image super-resolution using very deep residual channel attention networks, in: *Proceedings of the European conference on computer vision (ECCV)*, pp. 286–301.
- [48] Zhang, Y., Tian, Y., Kong, Y., Zhong, B., Fu, Y., 2018c. Residual dense network for image super-resolution, in: *Proceedings of the IEEE conference on computer vision and pattern recognition*, pp. 2472–2481.
- [49] Zhou, J., He, D., Shang, X., Guo, Z., Chen, S.L., Luo, J., 2021. Photoacoustic microscopy with sparse data by convolutional neural networks. *Photoacoustics* 22, 100242.
- [50] Zhu, X., Huang, Q., DiSpirito, A., Vu, T., Rong, Q., Peng, X., Sheng, H., Shen, X., Zhou, Q., Jiang, L., et al., 2022. Real-time whole-brain imaging of hemodynamics and oxygenation at micro-vessel resolution with ultrafast wide-field photoacoustic microscopy. *Light: Science & Applications* 11, 138.
- [51] Zhu, Y., Zhang, Y., Bonev, B., Yuille, A.L., 2015. Modeling deformable gradient compositions for single-image super-resolution, in: *Proceedings of the IEEE Conference on Computer Vision and Pattern Recognition*, pp. 5417–5425.
- [52] Zong, W., Wu, R., Li, M., Hu, Y., Li, Y., Li, J., Rong, H., Wu, H., Xu, Y., Lu, Y., et al., 2017. Fast high-resolution miniature two-photon microscopy for brain imaging in freely behaving mice. *Nature methods* 14, 713–719.